of 10 km, this gives a slip of 2.9 m for 1.2 m of slip at Loma Prieta ($x \approx 3$ km). A more precise three-dimensional dislocation calculation yields a slip of 2.5 ± 0.4 m from the surface to 10 km.

9. M. Lisowski, W. H. Prescott, J. C. Savage, M. J. Johnston, *Geophys. Res. Lett.* **17**, 1437 (1990).
10. T. A. Clark *et al.*, *ibid.*, p. 1215.
11. The EDM measurements were made to station Eagle; the GPS occupations were at Eagle Un, ~40 m away. In the calculation the two markers were treated as one. On Loma Prieta the GPS occupations and the south-directed EDM lines were from LP1, whereas the EDM lines to the north were from Loma USE. We have corrected all measurements to LP1. For this solution there are 59 observations, 46 unknowns (2 for each of 23 stations), and no null space.
12. For strike slip on a vertical dislocation extending from the earth's surface to depths of 5 to 15 km, the mean-square lack of fit [the residual sum of squares corrected for misclosure; see (*4*)] is 1.4. For strike slip on a plane dipping 70° to the southwest the mean-square lack of fit is 1.5. Both models provide acceptable fits to the data. W. Thatcher and G. Marshall [*Eos* **17**, 554 (1990)] presented similar results. In contrast, if the slip vector is constrained so that the strike-slip component is 1.4 times the dip-slip component, the mean-square lack of fit is 2.8, a significantly poorer fit. With 18 linearly independent observations and three parameters, models with mean-square lack of fit greater than 1.7 are rejectable at the 95% confidence level. The variance in the triangulation measurements estimated from the network misclosure is completely consistent with the a priori estimate of the data variance.
13. Near Loma Prieta a total of 33 to 38 mm/yr of slip is partitioned between the San Andreas and Calaveras faults. Estimates of slip on the San Andreas fault range from 13 mm/yr [W. H. Prescott, M. Lisowski, J. C. Savage, *J. Geophys. Res.* **86**, 10,853 (1981)] to 26 mm/yr [M. Matsa'ura, D. D. Jackson, A. Cheng, *ibid.* **91**, 12,661 (1986)].
14. W. C. Bradley and G. B. Griggs [*Geol. Soc. Am. Bull.* **87**, 433 (1976)] estimated uplift rates of as much as 0.26 mm/yr. T. C. Hanks, R. C. Bucknam, K. R. Lajoie, and R. E. Wallace [*J. Geophys. Res.* **89**, 5771 (1984)] estimated an uplift rate of 0.35 mm/yr. All rates apply to the Santa Cruz coastline, the uplift rate at the fault trace is not well known.
15. R. S. Anderson, *Science* **249**, 397 (1990); Valensise and Ward, in preparation.
16. The average rate of slip on the San Andreas fault in the Carrizo Plains has been 33.9 ± 2.9 mm/yr during the last 3,700 years and 35.8 + 5.4/−4.1 mm/yr during the last 13,250 yr [K. E. Sieh and R. H. Jahns, *Geol. Soc. Am. Bull.* **95**, 883 (1984)]; the geodetically determined slip-rate somewhat northwest on the creeping segment of the fault has been 33 ± 1 mm/yr over the last 100 years [W. Thatcher, *J. Geophys. Res.* **84**, 2283 (1979)].
17. J. Olson, *Geophys. Res. Lett.* **17**, 1492 (1990).
18. As pointed out by T. Heaton (personal communication). Erect a coordinate system with x'_1 horizontal and normal to fault strike, x'_2 horizontal and parallel to fault strike, and x'_3 vertical. The condition that the vertical fault be pure strike-slip is $\sigma'_{13} = 0$. If we assume that one principal stress is near vertical, then σ'_{23} must also vanish. The horizontal and vertical shear stresses acting on the dipping fault are given by $\tau_h = \sigma'_{12}\sin(\delta)$ and $\tau_v = (\sigma'_{11} - \sigma'_{33})\sin(\delta)\cos(\delta)$, where δ is the fault dip. Consider the intermediate principal stress (σ_2) to be vertical and the minimum compression (σ_3) to be at an angle θ clockwise from x'_1. The observed rake of the slip vector in the Loma Prieta earthquake requires that $\tau_h = \beta\tau_\nu$; $\beta \sim 1.4$ or $\phi = \sin^2(\theta) - \sin(\theta)\cos(\theta)/\beta\cos(\delta)$ where the parameter $\phi \equiv (\sigma_2 - \sigma_3)/(\sigma_1 - \sigma_3)$ describes the shape of the stress ellipsoid. Note that $\phi \geq 0$, as required by definition, for $\theta \geq \tan^{-1}[1/\beta\cos(\delta)] \approx 64°$. The direction of maximum compression, consistent with the slip vector in the two earthquakes, ranges from $64° \leq \theta < 90°$. The minimum value of θ (N16°E) occurs when $\sigma_2 = \sigma_3$, the maximum (N42°E) when $\sigma_2 = \sigma_1$.
19. A. G. Lindh, *U.S. Geol. Surv. Open-File Rep. 83-63* (1983); L. R. Sykes and S. P. Nishenko, *J. Geophys. Res.* **89**, 5905 (1984); C. H. Scholz, *Geophys. Res. Lett.* **12**, 17 (1985).
20. H. Kanamori (personal communication) pointed out that the two 1985 Nahani earthquakes, M_s 6.6 (October 1985) and M_s 6.9 (December 1985) had epicenters only 2 to 3 km apart, coincident aftershock zones, and similar focal mechanisms; these common features suggest that they either ruptured the same plane or closely spaced parallel planes; R. J. Wetmiller *et al.*, *Bull. Seismol. Soc. Am.* **78**, 590 (1988); G. L. Choy and J. Boatwright, *ibid.*, p. 1627.
21. We thank R. Kovach, T. Heaton, and H. Kanamori for valuable discussions; D. Richards, C. Williams, and Y. Du for assistance in the numerical calculations; J. Savage, W. Thatcher, D. Oppenheimer, G. Beroza, B. Ellsworth, and K. Lajoie for comments. This work was supported by the U.S. Geological Survey and by National Science Foundation grant EAR 90-03575 to Stanford University.

23 July 1990; accepted 19 October 1990

Modern Cyanobacterial Analogs of Paleozoic Stromatoporoids

JÓZEF KAŹMIERCZAK AND STEPHAN KEMPE

Recent and subfossil calcareous structures resembling cystose and subclathrate Paleozoic stromatoporoids have been discovered in a sea-linked, stratified, alkaline crater lake on Satonda Island, Indonesia. The structures are produced by mats of coccoid cyanobacteria growing along the lakeshore from the water surface down to the O_2-H_2S interface located at a depth of 22.8 meters. Calcification of the mats is controlled by seasonal changes in calcium carbonate supersaturation in the epilimnion. The internally complex structures are a product of two different calcification processes: (i) periodic in vivo calcification of the surficial cyanobacterial layers by low-Mg calcite, and (ii) early postmortem calcification of the cyanobacterial aggregates below the mat surface by microbially precipitated aragonite. The finding supports the idea that Paleozoic stromatoporoids represent fossilized cyanobacteria (stromatolites). It also implies that the stromatoporoid-generating epicontinental seas during the early Paleozoic may have been more alkaline and had a higher carbonate mineral supersaturation than modern seawater.

STROMATOPOROIDS ARE CALCAREOUS marine fossils common in many lower Paleozoic shallow-water carbonate deposits. The characteristic specimens came from Devonian limestones in Germany (*1*). These true stromatoporoids occur in mid-Ordovician to lowermost Carboniferous (Strunian) rocks. Most of the upper Paleozoic and Mesozoic fossils ascribed to stromatoporoids are sponges, predominantly calcified demosponges known as sclerosponges or coralline sponges (*2, 3*). They differ significantly from the Paleozoic stromatoporoids in their skeletal architecture, microstructure, and in the presence of spicules. Such pseudo-stromatoporoid fossils have been usually treated as separate groups and have been variously named Disjectoporida, Sphaeractinoidea, and Spongiomorphida (*4*). The practice of calling them stromatoporoids (*3, 5, 6*) should be abandoned because it is misleading.

Paleozoic stromatoporoids have been ascribed to various groups of organisms, in recent years to coelenterates (mostly hydrozoans) (*7*) and sponges (particularly sclerosponges) (*8*). No conclusive evidence for such affinities has been presented, however. Stromatoporoids have also been hypothesized (*9*) to form from in vivo calcification of coccoid cyanobacterial mats comparable to certain fossil and recent calcareous stromatolites. This suggestion has been supported by findings of remnants of coccoid cyanobacteria within skeletal elements of various stromatoporoids (*10*). Because living stromatoporoid-like stromatolites have not been found, the main question of this hypothesis is how the calicifying mats could produce the diversified and in many cases quite regular patterns that characterize many stromatoporoids. Some workers have suggested that these patterns are too advanced to be products of prokaryotic organisms (*11*).

In this report we describe modern calcified cyanobacterial mats that closely resemble certain Paleozoic stromatoporoids. These mats were discovered in the crater lake on Satonda Island (Indonesia) during the Indonesian-Dutch SNELLIUS II Expedition in November 1984, and we studied them in detail during the Indonesian-German SONNE 45B cruise in the fall of 1986 (*12*).

Satonda Island, ~2 km in diameter, is

J. Kaźmierczak, Institute of Paleobiology, Polish Academy of Sciences, Al. Zwirki i Wigury 93, PL-02089 Warszawa, Poland.

S. Kempe, Institute of Biogeochemistry and Marine Chemistry, University of Hamburg, Bundesstrasse 55, D-2000 Hamburg 13, Germany.

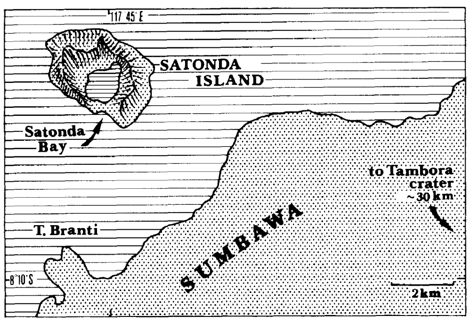

Fig. 1. Index map to Satonda Island, Indonesia.

located about 2.5 km offshore Sumbawa, northwest of the famous Tambora volcano (Fig. 1). Its central part is occupied by a seawater-filled crater lake 1.2 by 0.9 km wide. The steep slopes of the crater rim rise up to 300 m above lake level. The lake is 44 m deep on average and has a central plain 60 to 69 m deep. Satonda volcano has not been active for several thousand years. It was, however, covered by 50 to 80 cm of ash and pumice from the April 1815 cataclysm of Tambora.

The lake is midwater stratified (*12*) by a pronounced pycnocline at a depth of 22.8 m that separates an oxic epilimnion, 12.5% less salty than seawater, from an anoxic hypolimnion, 4.5% more saline than seawater. The oxic layer has a partial pressure of CO_2 (p_{CO_2}) in equilibrium with that of the atmosphere (~350 ppmv); whereas, in the anoxic layer, p_{CO_2} increases to up to 240,000 ppmv at depth. The dissolved inorganic carbon gave $\delta^{13}C$ values of −8.4, −11.4, and −21.4 per mil PDB (*13*) from depths of 10, 40, and 60 m, respectively. These negative values strongly suggest that the main source of the high p_{CO_2} is organic matter washed in from the crater rim. Reduction of sulfate to H_2S and the production of HCO_3^- or dissolution of fresh volcanic silicates under high p_{CO_2} has increased the total alkalinity in the crater lake. In the epilimnion it reaches 3.5 to 3.6 meq/kg (the alkalinity of seawater is 2.1 meq/kg), and it increases to 48 meq/kg at the lake bottom. The *p*H at the lake surface reaches 8.42, significantly higher than in normal surface seawater. The constant withdrawal of $CaCO_3$ by the calcifying cyanobacterial mats has lowered the Ca concentration to about half and the Mg concentration to about 85% of the values in seawater and increased the Mg/Ca molar ratio to 8 to 9 (the ratio of seawater is 5). Because of the high alkalinity and in spite of the low Ca concentration, the epilimnion is highly supersaturated with respect to carbonate minerals: the saturation indices (*14*) reach 0.70 for aragonite, 0.84 for calcite, and 2.81 for dolomite [Table 1, sample from 10 m depth, calculated with WATEQ (*15*)]. These conditions favor the chemical precipitation of aragonite and low-Mg calcite (*16*). The stromatolitic carbonate is precipitated nonenzymatically, that is, it shows the typical shifts of about +5 per mil toward higher $\delta^{13}C$ values (13 samples, mean ± SD = −3.5 ± 1.0 per mil) compared to dissolved carbonates [−8.4 per mil (*12*)].

The history of the crater lake and of its stromatolites is complex. Beneath the calcareous mounds we found organic mud; the presence of this mud indicates that the crater was originally filled with fresh water. Wood from that layer yielded a ^{14}C age of 3920 ± 30 years ago. We believe that at that time, part of the crater wall collapsed and seawater infiltrated through the remnant of the crater wall, which was less than 20 m wide. The lake was colonized by marine gastropods (*Ocenebra*, *Nerita*, and *Cerithium*) and pelecypods (*Pinctada* and perhaps *Lioconcha*). Eventually the bottom layer turned anoxic and produced excess alkalinity, which probably through eddy diffusion significantly alkalized the epilimnion. As the lake became alkaline, the marine mollusks would have been forced into extinction quickly. The alkaline environment apparently favored the growth of calcifying cyanobacterial mats. On rocky grounds along the lakeshore, 13 large stromatolitic reefs have been formed. They are more than 1 m thick and occur as low mounds and irregular crusts forming steep and partly overhanging walls down to the present O_2-H_2S interface at depths >23 m.

The next event in the lake's history was uplift of the island by >1 m after 310 ± 50 years ago (^{14}C dates of uplifted beach deposits). This uplift forced the beach line to recede ~100 m and ended the hydraulic connection between lake and sea. Input of rainwater would have diluted the surface layer and established a new pycnocline at midwater depths (which probably sank gradually to its present depth at 22.8 m).

Today the lake level stands 1.8 m above the highest sea level in the wet season and 0.8 m above it at the end of the dry season. Dilution of surface waters by rainfall has enhanced colonization of red algae (*Peyssonnelia* and *Lithoporella*), nubecullinid foraminifera, and serpulids, which, together with the coccoid cyanobacteria, form the present living reef surface. This association is overgrown down to 8 m depth by a thick carpet of filamentous green algae (siphonocladaleans), which themselves do not calcify. A large population of small cerithiid gastropods (*Rhinoclavis sinensis*) grazes on the cyanobacteria and green algae. Down to the O_2-H_2S interface the reef surface is densely overgrown by monaxonid demosponges (*Suberites* sp.).

The living surface of the calcified cyanobacterial mat has a pustular to cauliflower-like appearance to a depth of ~8 m, whereas deeper, it is almost smooth with occasional small protuberances. Analysis with the scanning electron microscope (SEM) shows that the mat surface is dotted with numerous fine tubercles that are typically located on more or less regularly distributed larger knobs (Fig. 2, A and B). The living zone of the mat is composed of a thin layer of subglobular aggregates of coccoid cyanobacteria (Fig. 2, B and C), which, according to current classification (*17*), can be assigned to the *Pleurocapsa* group. The gelatinous capsules (sheaths) surrounding groups of living pleurocapsalean cells are locally covered with anhedral granules of low-Mg calcite.

The weakly permineralized living cyanobacterial layers grade below the surface continously into a massive, finely laminated limestone composed of alternating micritic and sparitic sheets. These are visible in transmitted light as dark and light laminae, respectively. In the uppermost 3 to 5 cm of the crusts, the laminated structures occur as little nodules and thin interlayers between the foliaceous thalli of calcareous red algae.

Table 1. Chemical data of Satonda Crater Lake water; p_{CO2} and mineral saturation indices (SI) for aragonite (Ara), calcite (Cc), and dolomite (Dol) have been calculated with the program WATEQ (*15*); 1, sample from 10 m depth; 2, sample diluted by 5%; 3, dilution and decrease in temperature by 5°; 4 and 5, dilution, cooling, and p_{CO2} increase; 6, sample from 30 m; 7, sample from 30 m degassed to atmospheric p_{CO2}: 8, for comparison, seawater sample from Satonda Bay; *T*, temperature; Sal., salinity, Alk, alkalinity.

Parameter	1	2	3	4	5	6	7	8
T (°C)	29.9	29.9	25	25	25	29.8	29.8	29.5
Sal. (per mil)	30.87	29.32	29.32	29.32	29.32	36.82	36.82	34.37
*p*H	8.42	8.41	8.41	8.35	8.30	7.27	8.60	8.27
p_{CO2} (ppmv)	359	359	354	420	482	12040	340	289
Ca (mmol/kg)	5.42	5.15	5.15	5.15	5.15	6.47	6.47	10.6
Mg (mmol/kg)	42.17	40.06	40.06	40.06	40.06	50.11	50.11	50.11
C-Alk (meq/kg)	3.47	3.30	3.30	3.30	3.30	6.28	6.28	1.99
SI_{Ara}	0.70	0.66	0.62	0.57	0.54	−0.01	1.09	0.59
SI_{Cc}	0.84	0.80	0.76	0.72	0.68	0.13	1.23	0.73
SI_{Dol}	2.81	2.74	2.61	2.52	2.44	1.40	3.61	2.39

Fig. 2. (**A**) An SEM view of the slightly calcified living surface of the coccoid cyanobacterial mat from Satonda Crater Lake with fine tubercles and larger knobs; depth 9 m; scale bar is 500 μm. (**B**) Magnification of (A) showing globular capsules (sheaths) of the pleurocapsalean cell aggregates forming the mat and a few spicules of the monaxonid sponge (*Suberites* sp.) patchily overgrowing the cyanobacterial mat; scale bar is 100 μm. (**C**) Enlarged fragment of the above showing details of the living surface of the pleurocapsalean mat; scale bar is 30 μm. (**D**) Vertical section (transmitted light) of a subfossil part of a calcareous coccoid cyanobacterial buildup (microstromatolite) from Satonda Crater Lake. The lighter aragonitic layers alternate with darker calcitic layers arranged in a cystose to subclathrate pattern typical of some Paleozoic stromatoporoids. Arrow indicates cross section of a filament of siphonocladalean algae encrusted by cyanobacterial carbonate; sample was at water level; scale bar is 250 μm.

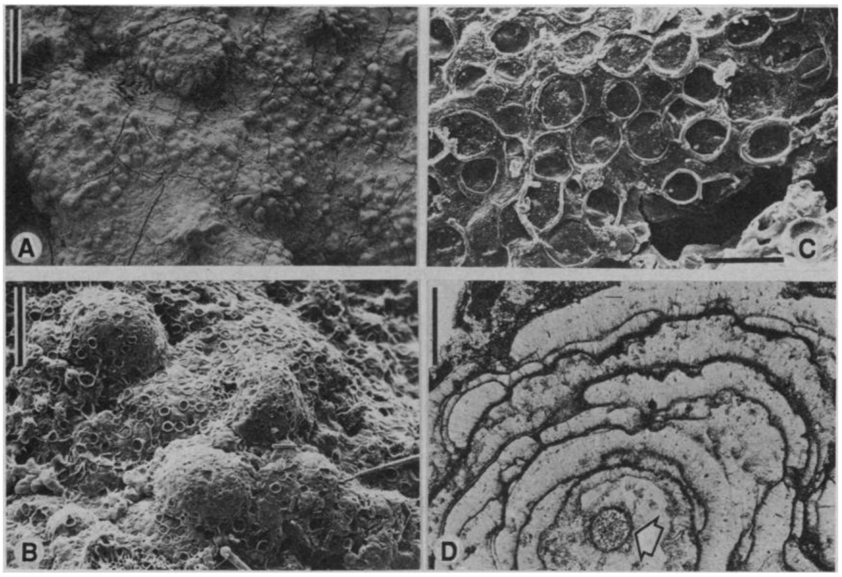

Farther down, the limestone is composed entirely of variously sized, elongated, and irregularly twisted laminated bodies mingled into a hard, massive rock. The center of each laminated body is occupied by typically one or rarely two or three empty, cylindrical tubes, 90 to 220 μm in diameter (Fig. 2D). The size and shape of these tubes indicate that they are molds of siphonocladalean thalli and are essentially similar to the filaments of *Cladophoropsis* associated with the living surface. The central position of the tubes in the laminated structures indicates that the siphonocladalean filaments originally formed the growth base of the laminated encrustations.

The dark laminae are much thinner (15 to 50 μm) than the light ones (20 to 300 μm) and are arranged in a subhorizontal to subcystose or cystose manner (Fig. 2D). At junctions between neighboring cysts, subvertical to vertical column- and pillar-like structures occur; the latter typically has a characteristic spool-like shape (Fig. 3A). Analysis by SEM and energy-dispersive x-ray mapping of EDTA-etched sections revealed that the dark and light laminae differ fundamentally both in microstructure and mineralogy. The dark laminae display an irregularly porous microstructure and are composed of low-Mg calcite, whereas the light ones are compact and made of fibrous aragonite (Fig. 3C).

The SEM analyses demonstrate that the subfossil laminated bodies are calcareous stromatolites (microbialites) produced by coccoid cyanobacteria identical to those forming the mat surface today. Remnants of these cyanobacteria are still identifiable in the dark as well as in the light laminae. In the dark laminae, clusters of coccoid microfossils representing capsules or molds of capsules of pleurocapsalean cyanobacteria are seen embedded in a granular, calcitic matrix (Fig. 3C). Similar if not identical capsules are known from other modern and fossil stromatolites (*10, 18*). In the light laminae, residues of the outer common sheaths (glycocalyx) that surround the coccoid cell aggregates in vivo can be identified in only a few samples. With careful etching of the aragonite laminae with EDTA, however, the traces of a continuous mass of coccoid aggregates became visible. These traces form rounded depressions that correspond in size and distribution to the better preserved pleurocapsalean aggregates from the dark laminae. This observation provides evidence of a uniform microbial origin of the entire stromatolitic structure.

We suggest that the following events lead to the observed laminated microstructure (Fig. 4). First, the cyanobacteria grow to dome-like aggregate a few hundred micrometers thick. Then the outer layer is mineralized in vivo by low-Mg calcite. Decay of the now encased inner aggregates by sulfate reduction increases the alkalinity beneath the calcitic cyst and triggers crystallization of aragonite. Thus the aragonite preserves largely decayed cell aggregates in contrast to the in vivo permineralized aggregates in the calcite layer. The interpretation of the aragonite as postmortem precipitate is substantiated by the occurrence of threadlike struc-

Fig. 3. (**A**) Vertical section (transmitted light) of the subfossil part of a calcareous microstromatolite from Satonda Crater Lake. It shows stromatoporoid-like arrangement of the darker calcitic components among which skeletal elements like cysts, laminae, spool-like pillars, and thicker columns typical of many Paleozoic stromatoporoids can be distinguished; sample was at water level; scale bar is 100 μm. (**B**) Enlarged micrograph of the above illustrating the mineralogical and textural differences between the in vivo (low-Mg calcite) and early postmortem (aragonite) permineralized coccoid cyanobacterial mat. Numerous filaments of saprotrophic fungi are visible in the aragonitic layer; scale bar is 50 μm. (**C**) SEM photomicrograph (vertical section, EDTA etching) of the contact between the calcitic and aragonitic laminae as shown in (B). Note the well-preserved capsules of pleurocapsalean cyanobacteria in the granular calcitic lamina and the fibrous character of the aragonitic lamina. Scale bar is 5 μm. (**D**) SEM picture (vertical section, EDTA etching) of an aragonitic lamina from the specimen shown in (B). Arrow indicates remnant of an almost totally decomposed coccoid cyanobacterial aggregate in the dense network of filaments of decomposing fungi and bacteria; scale bar is 25 μm.

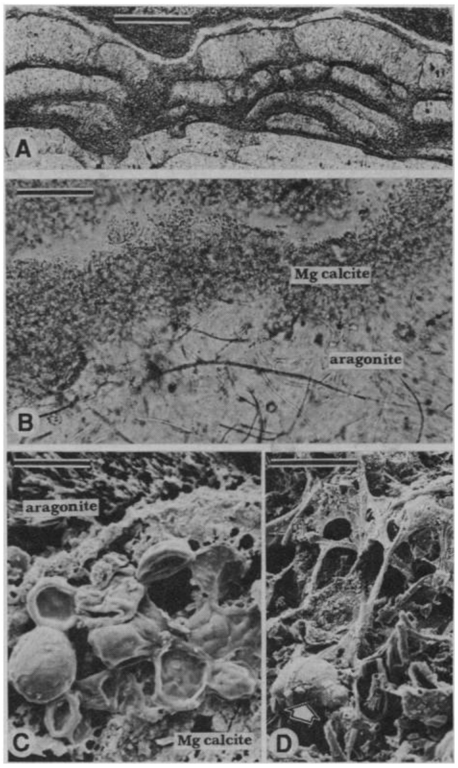

tures in this layer (Fig. 3, B and D) that closely resemble hyphae of saprotrophic fungi or sheaths of sulfur bacteria indicative of anaerobic decay. Calcification as a consequence of anaerobic decomposition by sulfate reduction is a well-known process below the zone of photosynthesis in modern cyanobacterial mats (*19*).

This model does not, however, answer why the coccoid aggregates can grow nonmineralized for some time and what triggers calcite precipitation on the mat surface. High $CaCO_3$ supersaturation is believed to be the crucial factor inducing in vivo calcification of cyanobacteria (*20*), although the deposition of $CaCo_3$ can be initiated in different ways (*21*). Fluctuations in supersaturation can be caused by changes in three factors: temperature, p_{CO_2}, and the concentrations of the Ca^{2+} and $CO_3{}^{2-}$. Satonda has two seasons: a cool rainy season and a hot dry season. During the rainy season the lake level rises by ~1 m, and the epilimnion could be diluted by about 5%. The lake probably also cools by a few degrees Celsius. At the same time, organic debris washed into the lake produces a temporary increase in p_{CO_2}.

We have calculated the effects of variations in the three factors on supersaturation (Table 1). These calculations show that supersaturations of aragonite and calcite can indeed be lowered to values comparable to their respective seawater supersaturations (column 8), that is, to values that apparently do not sustain in vivo calcification of the cyanobacterial mat. Under a reduced supersaturation, cyanobacteria might grow rapidly without triggering significant calcite precipitation (Fig. 4A). With warming and evaporation during the dry season, the critical calcite supersaturation (at about SI = 0.8) is surpassed and calcite is precipitated at the mat surface (Fig. 4B).

The calculations are valid only for the present conditions. The massive laminated bodies apparently formed, however, before the present epilimnion was established. Exact chemical conditions at that time are difficult to reconstruct. If one assumes that the water below the present pycnocline represents the former epilimnic water, one can calculate its supersaturation at atmospheric p_{CO_2} (Table 1, columns 7 and 8). The resulting supersaturations are large and would sustain spontaneous carbonate precipitation. These supersaturations are the consequence of a few hundred years of alkalinity increase caused by sulfate reduction and by dissolution of carbonate particles sinking into the anoxic bottom layer. Model calculations for the present epilimnic conditions illustrate that seasonal variations in supersaturations may be strong enough to cause the observed lamination in the cyanobacterial buildups.

The textural patterns observed closely resemble those described in many Paleozoic stromatoporoids. The similarity is particularly striking for the cystose, subcystose, and subclathrate stromatoporoids characterizing the initial, Ordovician, and the final, Fammenian-Strunian, periods in the history of the group. The Ordovician examples include stromatoporoids classified to *Cystostroma* (*22, 23*), *Pseudostylodictyon* (*22, 24, 25*), or *Clathrodictyon* (*23, 25, 26*); the Fammenian-Strunian examples include forms described as *Pseudolabechia* (*27*) or *Stylostroma* (*28*). Cystose and subcystose patterns remarkably similar to those occurring in Satonda stromatolites have also been described from early Proterozoic marine stromatolites (*29*) and Quaternary lacustrine microbial tuffas (*30*).

The dark laminae of the Satonda microbialites are similar to the skeletal elements of Paleozoic stromatoporoids, whereas the light laminae may correspond to interskeletal spaces. In fossil stromatoporoids, the spaces are filled with sparry low-Mg calcite that most likely originated from diagenetic transformation of primary aragonite or represents neospar filling the fenestral spaces remaining in the cyanobacterial mats after the decay of the noncalcified coccoid aggregates. The presence of primary aragonite in stromatoporoids has been suggested from studies on authigenic quartz inclusions in Devonian *Actinostroma* and *Stromatopora* (*31*). Also megaquartz crystals have been observed in Devonian stromatoporoids (*32*); the quartz is associated with closed spaces filled with organic material that acts as nucleating agent. All these observations are in agreement with the interpretation of stromatoporoid morphogenesis given above. Irregular stellate patterns (the so-called "astrorhizae") occurring in some stromatoporoids (*24*) are not present in the Satonda mats. The abundance of molds of filaments of siphonocladalean green algae in the stromatolites studied indicate, however, that such patterns could be easily produced by rhizoids or branched thalli of similar algae overgrown by the calcifying cyanobacterial mat.

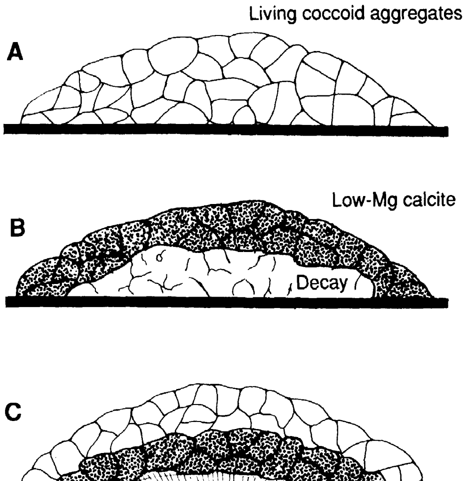

Fig. 4. Diagram illustrating major stages in the formation of an arcuate cyst plate in a cystose stromatoporoid-like calcareous stromatolite. (**A**) Dome-shaped aggregate of living coccoid cyanobacteria. (**B**) Periodic in vivo permineralization of the surficial cells with low-Mg calcite. The noncalcified coccoids remaining below the calcitic cyst have been obliterated by heterotrophic microorganisms post-mortem. (**C**) The metabolic activity of the decomposing microbiota mediates an early diagenetic formation of aragonite in the cryptic microenvironment.

The species-poor biota of the mildly alkaline Satonda Crater Lake parallels the low or even extremely low diversity biota associated with the extensive stromatoporoid banks and mounds that characterize the Silurian and Devonian carbonate platforms worldwide (*33*). Considering the devastating impact of alkaline seawater on the marine mollusks that once lived in Satonda lake, we conclude that a similar increase in alkalinity accompanied by changes in the main ionic composition may also have caused temporal impoverishment of normal marine organisms and enhanced development of in vivo calcifying stromatoporoid-like cyanobacterial mats in the early Paleozoic epicontinental seas. All cyanobacteria are alkaliphilic microorganisms (*34*), and their abundance can be taken per se to indicate that an environment is alkaline. At Satonda Crater Lake, the generation of stromatoporoid-like stromatolites requires, in addition to increased alkalinities, fluctuations in $CaCO_3$ supersaturation levels. The widely accepted models of stratified or sluggish early Paleozoic seas (*35*) imply that similar conditions may have produced stromatoporoids there. Deeper, anoxic basins of those epicontinental seas could have easily produced excess alkalinity, and these waters, through temporal destratification of the water column or upwelling systems, could have periodically invaded the shallow areas and generated high $CaCO_3$ supersaturation levels that promote the formation of stromatoporoid stromatolites. The periodic changes in $CaCO_3$ supersaturation combined with other changing environmental factors important for cyanobacterial growth such as O_2 and $PO_4{}^{3-}$ levels, temperature, and light intensities could alter the organization of cyanobacterial colonies and produce a plethora of mat configurations.

A large number of textural patterns have been produced by the temporally in vivo calcifying mats. On the basis of these textures, taxonomists have designated over

2000 species of Paleozoic stromatoporoids (*36*). Compared to their Satonda counterparts, the Paleozoic stromatoporoids are characterized by generally thicker growth increments and more regular textures that sometimes show almost perfect superposition of pillars and columns. This texture could have been caused by a larger temporal and spatial persistence of regular fluctuations in the Paleozoic seas compared to the hydrochemically less stable and geologically short-lived Satonda Crater Lake.

Stromatoporoids apparently survived the Frasnian-Fammenian crisis and became extinct during the lowermost Carboniferous (Strunian). Their disappearance has been mostly attributed to ocean cooling or meteorite impact (*37*). From our studies on Satonda stromatolites we suggest that a worldwide decrease in alkalinity and in carbonate mineral supersaturation following the Fammenian oceanic turnover (*38*) may better account for the fading of stromatoporoid stromatolites from the late Paleozoic geological record.

REFERENCES AND NOTES

1. A. Goldfuss, *Petrefacta Germaniae*, vol. I (Arnz, Düsseldorf, 1826).
2. J. Kaźmierczak, *Palaeontology* **17**, 341 (1974).
3. R. A. Wood, *Spec. Pap. Palaeontol.* **37**, 1 (1987); ———, J. Reitner, R. R. West, *Lethaia* **22**, 85 (1989).
4. O. Kühn, in *Handbuch der Paläozoologie*, O. H. Schindewolf, Ed. (Borntraeger, Berlin, 1939), vol. 2A, pp. 3–68; E. Flügel, *Palaeontol. Z.* **49**, 369 (1975).
5. Y. Dehorne, *Mém. Serv. Explication Carte Géol. Detaill. France* (1920); H. Yabe and T. Sugiyama, *Sci. Rep. Tohoku Imp. Univ. Sendai Ser. 2* **14**, 135 (1935); R. G. S. Hudson, *Palaeontology* **2**, 180 (1960).
6. R. A. Wood and J. Reitner, *Palaeontology* **29**, 469 (1986); J. Wendt, *Neues Jahrb. Geol. Palaeontol. Abh.* **150**, 111 (1975).
7. H. Nestor, *Lethaia* **14**, 21 (1981); K. Mori, *Stockholm Contrib. Geol.* **37**, 167 (1982); O. V. Bogoyavlenskaya, *Stromatoporaty Paleozoya* (Nauka, Moscow, 1984).
8. W. D. Hartman and T. E. Goreau, *Symp. Zool. Soc. London* **25**, 205 (1970); C. W. Stearn, *Lethaia* **5**, 369 (1972).
9. J. Kaźmierczak, *Nature* **264**, 49 (1976).
10. ———, *Acta Palaeontol Pol.* **25**, 243 (1980; ——— and W. E. Krumbein, *Lethaia* **16**, 207 (1983).
11. R. Riding and S. Kershaw, *Nature* **268**, 178 (1977); C. T. Scrutton, in *The Origin of Major Invertebrate Groups*, M. R. House, Ed. (Academic Press, London, 1979), pp. 167–207; C. Monty, in *Phanerozoic Stromatolites*, C. Monty, Ed. (Springer, Berlin, 1981), pp. v–viii.
12. S. Kempe and J. Kaźmierczak, *Chem. Geol.* **81**, 299 (1990).
13. $\delta^{13}C = [(^{13}C_{sample}/^{12}C_{sample})/(^{13}C_{PDB}/^{12}C_{PDB})]1000$, where PDB is the Pee Dee Belemnite standard.
14. The saturation index (SI) is defined as $\log [(IAP)/K_{mineral}]$, that is for calcite (Cc): $\log([Ca^{2+}][CO_3^{2-}]/K_{Cc})$; IAP = ion activity product.
15. L. N. Plummer, B. F. Jones, A. H. Truesdell, *U.S. Geol. Surv. Water Res. Invest. Pap. 76-13* (1976; revised 1978, 1984).
16. G. Müller, G. Irion, U. Förstner, *Naturwissenschaften* **59**, 158 (1972); R. L. Folk, *J. Sediment. Petrol.* **44**, 40 (1974).
17. R. Rippka, J. W. Waterbury, R. Y. Stanier, in *The Prokaryotes*, M. P. Starr *et al.*, Eds. (Springer, Berlin, 1981), vol. 1, pp. 247–256.
18. R. J. Horodyski and S. Vonder Haar, *J. Sediment. Petrol.* **45**, 894 (1975); W. E. Krumbein and C. Giele, *Sedimentology* **26**, 593 (1979); C. J. R. Braithwaite, J. Casanova, T. Frevert, B. A. Whitton, *Palaeogeogr. Palaeoclimatol. Paleoecol.* **69**, 145 (1988).
19. W. E. Krumbein and Y. Cohen, in *Fossil Algae*, E. Flügel, Ed. (Springer, Berlin, 1977), pp. 37–56; W. E. Lyons *et al.*, *Geology* **12**, 623 (1984).
20. K. Simkiss, in *Biomineralization in Lower Plants and Animals*, B. S. C. Leadbeater and R. Riding, Eds. (Clarendon, Oxford, 1986), pp. 19–37; S. Kempe and J. Kaźmierczak, in *Facets of Modern Biogeochemistry*, V. Ittekkot, S. Kempe, W. Michaelis, A. Spitzy, Eds. (Springer, Berlin, 1990), pp. 252–275.
21. W. E. Krumbein, in *Biogeochemical Cycling of Mineral-Forming Elements*, P. A. Trudinger and D. J. Swaine, Eds. (Elsevier, Amsterdam, 1979), pp. 47–68; A. Pentecost, *Geomicrobiol. J.* **4**, 285 (1985); A. Pentecost and J. Bauld, *ibid.* **6**, 129 (1988).
22. J. J. Galloway and J. St. Jean, Jr., *Bull. Am. Paleontol.* **43**, 5 (1961).
23. T. E. Bolton, *Geol. Surv. Can. Bull.* **379**, 17 (1988).
24. J. J. Galloway, *Bull. Am. Paleontol.* **37**, 345 (1957).
25. H. E. Nestor, *Ordovician and Llandoverian Stromatoporoidea of Estonia* (Valgus, Tallinn, 1964).
26. B. D. Webby, *Palaeontology* **12**, 637 (1969).
27. C. W. Stearn, *J. Paleontol.* **62**, 411 (1988).
28. D. Y. Dong, *Acta Palaeontol. Sin.* **12**, 280 (1964).
29. M. R. Walter, in *Earth's Earliest Biosphere*, J. W. Schopf, Ed. (Princeton Univ. Press, Princeton, 1983), pp. 187–213.
30. J. Casanova, *Sci. Géol. Bull.* **40**, 135 (1987); C. Hilaire-Marcel and J. Casanova, *Palaeogeogr. Palaeoclimatol. Palaeoecol.* **58**, 155 (1987).
31. D. K. Richter, *Sedimentology* **19**, 211 (1972).
32. R. A. Henderson, *J. Sediment. Petrol.* **54**, 1138 (1984).
33. L. F. Laporte, Ed., *Soc. Econ. Paleontol. Mineral. Spec. Publ.* **18** (1974); D. F. Toomey, Ed., *ibid.* **30**, (1981).
34. T. D. Brock, *Science* **179**, 480 (1973).
35. W. B. N. Berry and P. Wilde, *Am. J. Sci.* **278**, 257 (1978); P. Wilde and W. B. N. Berry, *Palaeogeogr. Palaeoclimatol. Palaeoecol.* **48**, 143 (1984); W. T. Holser, M. Magaritz, J. Wright, in *Global Bio-Events*, O. Walliser, Ed. (Springer, Berlin, 1986), pp. 63–74; J. Wright, H. Schrader, W. T. Holser, *Geochim. Cosmochim. Acta* **51**, 631 (1987).
36. E. Flügel and E. Flügel-Kahler, in *Fossilium Catalogus*, I. F. Westphal, Ed. (Jung, Gravenhage, 1968), pp. 1–681.
37. P. Copper, *Geology* **14**, 835 (1986); C. W. Stearn, *ibid.* **15**, 677 (1987); D. J. McLaren, *ibid.* **13**, 170 (1985).
38. H. H. J. Geldsetzer, W. D. Goodfellow, D. J. McLaren, M. J. Orchard, *Geology* **15**, 393 (1987); U. Brand, *Palaeogeogr Palaeoclimatol. Palaeoecol.* **76**, 311 (1989).
39. We thank G. Landmann, A. Lipp, Y. Surachman, and D. Susanto for field assistance. The paper has been reviewed by H. K. Wong, W. E. Krumbein, and A. Nissenbaum. Supported by the German Federal Ministry of Research and Technology, Polish Academy of Sciences, and a fellowship from the A. V. Humboldt Foundation (to J.K.). The paper is a contribution to the IGCP Project No. 261, "Stromatalites."

15 May 1990; accepted 22 August 1990

Simulation of Tsunamis from Great Earthquakes on the Cascadia Subduction Zone

MAX K.-F. NG, PAUL H. LEBLOND,* TAD. S. MURTY

Large earthquakes occur episodically in the Cascadia subduction zone. A numerical model has been used to simulate and assess the hazards of a tsunami generated by a hypothetical earthquake of magnitude 8.5 associated with rupture of the northern sections of the subduction zone. Wave amplitudes on the outer coast are closely related to the magnitude of sea-bottom displacement (5.0 meters). Some amplification, up to a factor of 3, may occur in some coastal embayments. Wave amplitudes in the protected waters of Puget Sound and the Strait of Georgia are predicted to be only about one fifth of those estimated on the outer coast.

THE CASCADIA SUBDUCTION ZONE IS the area where the Juan de Fuca plate and smaller adjacent plates slip below the North American continent (Fig. 1). The possibility of a massive earthquake in this area has recently been recognized (*1*). A seismic sea wave, or tsunami, would be a major risk associated with such an event. In this report, we present calculations that quantify this risk and allow identification of the factors that would determine flooding levels along the adjacent coast.

A critical element in tsunami modeling is the nature of the initial sea-level displacement that starts the wave. Because the rupture takes place on a time scale that is short compared to the response time of the ocean waters, the sea-surface displacement, which causes the tsunami, is practically identical to that of the sea bottom. Geophysical arguments (*2*) suggest that a vertical uplift of 5 m of the ocean bottom along the deformation front, decreasing linearly to zero at the coast line, is possible during a large earthquake. We have modeled only the rupture of the northern sections of the Cascadia subduction zone (north of 48°N). A maximum earthquake magnitude of 8.2 is estimated for rupture of each of the Winona and Explorer segments and of about 8.5 for simultaneous rupture of all segments north of 48°N (Fig. 1).

Tsunami propagation from an impulsive

M. K.-F. Ng and P. H. LeBlond, Department of Oceanography, University of British Columbia, Vancouver, BC Canada V6T 1W5.

T. S. Murty, Institute of Ocean Sciences, Post Office Box 6000, Sidney, BC Canada V8L 4B2.